Supporting Information for

$O(^3P)$ + CO_2 collisions at hyperthermal energies: Dynamics of non-reactive scattering, oxygen isotope exchange, and oxygen-atom abstraction

Laurence Y. Yeung, Mitchio Okumura, Jianming Zhang, Timothy K. Minton,* Jeffrey T. Paci, Amir Karton, Jan M. L. Martin, Jon P. Camden, and George C. Schatz**

Table S1. Diagnostics related to the importance of nondynamical correlation.

	%TAE*e* [a]				CCSD(T)/aug'cc-pVTZ	
	[SCF]	[(T)]	post-CCSD(T)	[T_4 + T_5]	T_1 [b]	D_1 [c]
O_2	22.3	7.7	0.36	0.97	0.007	0.013
CO	70.0	3.1	0.04	0.26	0.019	0.039
CO_2	66.3	3.6	0.02	0.29	0.018	0.047
$CO_3(^3A')$	54.2	5.0	0.36	0.55	0.022	0.074
$CO_3(^3A'')$	50.9	5.7	1.05	0.99	0.035	0.108
$TS1(^3A')$	52.2	5.7	0.31	0.51	0.044	0.144
$TS1(^3A'')$	54.8	5.5	0.41	0.53	0.056	0.242
$TS2(^3A'')$	46.6	6.1	0.42	0.63	0.035	0.096
$TS3(^3A'')$	43.5	6.6	0.70	0.78	0.043	0.147

[a] Percentages of the total atomization energy related to nonrelativistic, clamped-nuclei values with inner shell electrons constrained to be doubly occupied. The %TAE*e*[(T)] diagnostic was found to provide a better correlation with the magnitude of post-CCSD(T) contributions than the T_1 and D_1 diagnostics (see Refs. 1 and 2 for further details).
[b] See Ref. 3.
[c] See Ref. 4.

Benchmarking W4 energies: O(^3P) + HCl

The results from W4 calculations for the benchmark O(^3P) + HCl reaction are listed in Tables S2 and S3. The results from B3LYP/6-311G(d), BMK/6-311G(d), and CCSD(T)/aug-cc-pVTZ levels of theory are also listed in Table S2 for comparison. Figure S1 shows the $^3A''$ PES along with the CCSD(T)/aug-cc-pVTZ geometries of the two transition states (O_HCl_TS1 and O_HCl_TS2) connecting the reactants with Cl + OH and ClO + H, respectively. At the W4 level, the O + HCl $\rightarrow$ Cl + OH reaction is almost thermoneutral: at the bottom of the well it is slightly exothermic (ΔE_e = –0.6 kcal mol^{-1}) and when the zero point vibrational energy is added it becomes slightly endothermic (ΔE_0 = +0.4 kcal mol^{-1}).[5] The ClO product channel is endothermic by as much as 42.0 kcal mol^{-1} at the bottom of the well.

Table S2 shows that the CCSD(T)/aug-cc-pVTZ barriers for the OH and ClO product channels overestimate the CCSD(T) basis set limit barriers by 0.5 and 2.5 kcal mol^{-1}, respectively. The CCSD(T) basis set limit barriers overestimate the FCI basis set limit barriers by 1.2 and 0.9 kcal mol^{-1}, respectively. Turning to the DFT results, we note that the BMK/6-311G(d) barrier for the OH product channel is only 0.2 kcal mol^{-1} below the FCI basis set limit value, but the barrier for the ClO product channel is overestimated by 5.8 kcal mol^{-1}. Whereas

the B3LYP/6-311G(d) barrier for the ClO product channel is nearly the exact FCI basis set limit value, the barrier for the OH product channel is underestimated by 6.2 kcal mol^{-1}. Similar to the O(^3P) + CO_2 system, we see (Table S3) that both the T_3–(T) and T_4 contributions reduce the barrier heights by chemically significant amounts: 0.6 and 0.6 kcal mol^{-1} for the OH product channel, and 0.5 and 0.4 kcal mol^{-1} for the ClO product channel. Finally, we note that the DBOC contribution to the barriers ranges between 0.1 – 0.2 kcal mol^{-1}.

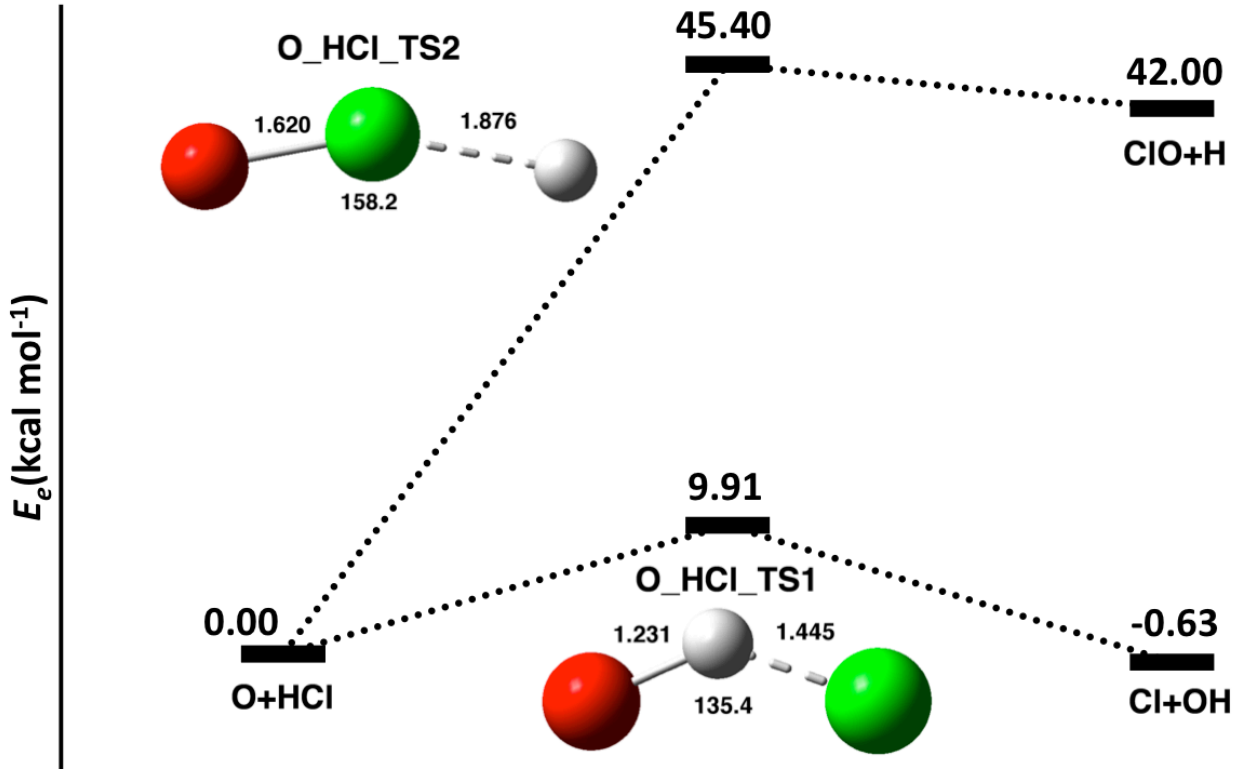

Figure S1. W4 PES at the bottom of the well (in kcal mol^{-1}) for the O(^3P) + HCl reaction (the CCSD(T)/aug-cc-pVTZ geometries of the transition states are given in Angstroms and degrees, respectively).

Table S2. Energies (kcal mol^{-1}, relative to the free reactants) for the stationary points on the lowest triplet PES for the $O(^3P)$ + HCl reaction.

	B3LYP/ 6-311G(d)	BMK/ 6-311G(d)	CCSD(T)/ aug-cc-pVTZ	W4 CCSD(T) Limit[a]	W4 FCI Limit[b]	W4 FCI Limit[c]
O_HCl_TS1	3.41	9.43	11.26	10.74	9.54	9.60
Cl+OH	-1.33	0.29	0.59	0.31	0.23	0.28
O_HCl_TS2	45.05	50.93	48.42	45.98	45.04	45.15
ClO+H	43.85	46.05	44.98	42.88	42.19	42.21

[a]W4 zero-point exclusive, nonrelativistic, clamped-nuclei, valence CCSD(T) basis set limit.
[b]W4 zero-point exclusive, nonrelativistic, clamped-nuclei, valence FCI basis set limit.
[c]W4 zero-point exclusive, nonrelativistic, clamped-nuclei, all-electron FCI basis set limit for comparison with the DFT results.

Table S3. Component breakdown of the final W4 energies (kcal mol^{-1}) for O(^3P) + HCl at the bottom of the well.

	SCF	Valence CCSD	Valence (T)	T_3– (T)	T_4	T_5	Inner-shell	Relativistic	Spin-orbit	DBOC	M-A[a]	TAE_e
Total atomization energies												
ClO	9.53	48.57	6.35	0.04	0.62	0.02	0.17	-0.23	-0.61	0.00	0.03	64.46
HCl	80.85	25.00	1.48	-0.11	0.10	0.00	0.19	-0.25	-0.84	0.04	0.01	106.47
OH	69.29	36.02	1.70	-0.02	0.09	0.00	0.14	-0.12	-0.02	0.01	0.02	107.10
O+HCl_TS1(^{3}A″)	47.74	43.35	5.50	0.48	0.71	0.00	0.12	-0.14	-1.06	-0.15	0.01	96.56
Reaction energies												
O+HCl_TS2(^{3}A″)	-3.03	57.06	7.32	0.41	0.50	0.02	0.08	-0.11	-1.06	-0.13	0.03	61.07
HCl+O → OH+Cl	11.56	-11.02	-0.22	-0.09	0.01	0.00	0.05	-0.12	-0.82	0.03	-0.01	-0.63
HCl+O → ClO+H	71.32	-23.57	-4.87	-0.15	-0.52	-0.02	0.02	-0.01	-0.23	0.04	-0.02	42.00
Forward barriers												
HCl+O → O_HCl_TS1(^{3}A″)	33.11	-18.35	-4.02	-0.59	-0.61	0.00	0.07	-0.11	0.22	0.19	0.00	9.91
HCl+O → O_HCl_TS2(^{3}A″)	83.88	-32.06	-5.84	-0.52	-0.40	-0.02	0.11	-0.14	0.22	0.17	-0.02	45.40
Reverse barriers												
OH+Cl → O_HCl_TS1(^{3}A″)	21.54	-7.32	-3.80	-0.50	-0.62	0.00	0.02	0.01	1.04	0.16	0.01	10.54
H+ClO → O_HCl_TS2(^{3}A″)	12.56	-8.49	-0.97	-0.37	0.12	0.00	0.09	-0.13	0.45	0.13	0.00	3.40

[a]Difference between the MOLPRO and ACES II definitions of the valence ROCCSD(T); one half of this contribution is added to the final TAE as discussed in the appendix of Ref. 1.

Hyperthermal oxygen source

The hyperthermal oxygen beam was generated by laser detonation of a pulsed expansion of O_2 gas with 500 psig stagnation pressure using a source based on the design of Caledonia *et al*.[6] 174 μs after the pulsed valve is triggered, the CO_2 laser is fired; the laser pulse passed through an antireflection-coated ZnSe window into the source chamber, whereupon it was reflected back towards the gold-plated, water-cooled copper nozzle with a 1-m radius concave gold mirror. The focused laser pulse initiates a breakdown of the O_2 gas and heats the resulting plasma to > 20,000 K, which accelerates both the atomic and molecular oxygen fractions of the pulsed beam to 6 – 9 km s^{-1}. Use of a conical nozzle allowed for efficient ion-electron recombination and inefficient atom-atom and atom-molecule recombination as the plasma expanded and cooled. The resulting gas pulse was collimated by a 7-mm diameter aperture located 80 cm downstream of the inlet nozzle into a differentially pumped region (10^{-5} – 10^{-6} Torr), after which it passed through a 3.0-mm-diameter skimmer 16 cm further downstream. The beam interaction region was an additional 3 cm downstream in the main chamber (2×10^{-7} Torr), a total distance of 99 cm from the inlet nozzle.

For velocity selection within the hyperthermal oxygen beam, a chopper wheel running at 300 Hz (synchronized with the 2-Hz laser pulses) was placed inside the main scattering chamber, just downstream of the skimmer. Three equally-spaced slots (1.5 mm wide) of the chopper wheel pass over an LED/photodiode assembly a quarter-turn before each slot enters the beam axis, generating a 900 Hz (3 × 300 Hz) train of pulses. These chopper wheel pulses are sent to a digital delay generator and used as references for triggering the O_2 gas pulses. The time delay between the chopper wheel pulse and the O_2 pulse determined the portion of the overall hyperthermal oxygen beam allowed to pass through into the interaction region.

We characterized the velocity distribution of the hyperthermal oxygen beam under two conditions: on axis ($\Theta = 0°$) with a small aperture (~125 μm diameter) to obtain the peak of the distribution, and off axis ($\Theta = 3°$) with a large aperture (4 mm × 4 mm) to obtain the width of the distribution. For the on-axis configuration, a 2-mA emission current at the ionizer and a –18 kV potential at the secondary emitting electrode of the Daly ion counter was used. For the off-axis configuration, a 10-mA emission current at the ionizer and a –30 kV potential at the secondary emitting electrode was used. Laboratory TOF distributions under both conditions were

measured, for both ^{16}O and $^{16}O_2$, to determine the laboratory-frame velocities and translational energy distributions for the hyperthermal oxygen beam.

A pulsed supersonic expansion of neat $^{12}C^{18}O_2$ was generated using a piezoelectric pulsed general valve with a 1300 Torr stagnation pressure. The expansion passed through a 5-mm diameter skimmer (9.2 cm from the nozzle) into a differential pumping region, and then through a 3.0-mm diameter (2.8 cm downstream of the skimmer) aperture into the main scattering chamber. The distance from this aperture to the interaction region was 1.5 cm. The velocity distribution of the $^{12}C^{18}O_2$ beam was not measured directly; instead, it was determined iteratively by first estimating the terminal velocity of the supersonic expansion,[7] and then fitting the $^{12}C^{18}O_2$ velocity to the value that yielded the best Newton circle for non-reactively scattered O atoms, while keeping the measured O-atom velocity distribution fixed at its measured values. This contributes some uncertainty to the measured TOF distributions because the $^{12}C^{18}O_2$ beam velocity is accurate to approximately ±10%. However, because the O-atom beam speed was ten times that of the $^{12}C^{18}O_2$ beam and its FWHM was 4 – 5 times that of the $^{12}C^{18}O_2$ beam, uncertainties in the "time-zero" of the oxygen source dominated the uncertainty in the translational energy distributions.

Laboratory-to-c.m. frame coordinate transformation

A forward-convolution method was employed to perform the laboratory-to-c.m. frame coordinate transformation[7] of the data using the MSU XBEAM program (Version 6). Trial c.m. $P(E_T)$ and $T(\theta_{c.m.})$ distributions were used to simulate the laboratory-frame TOF distributions using the following relationship derived from the Jacobian transformation:

$$N(t,\Theta) \propto \frac{l^3}{ut^3} P(E_T) T(\theta_{c.m.})$$

where l and t are the distance and flight time, respectively, from the interaction region to the ionizer, and u is the product velocity in the c.m. frame. During the fitting process, the lab-frame $^{12}C^{18}O_2$ beam velocity was assumed to be a single value, 800 m s^{-1}, because the large magnitude and width of the hyperthermal oxygen beam velocity distribution is principally responsible (i.e., it contributed ≥ 98% of the uncertainty in the c.m. collision energy) for the observed width of the laboratory TOF distributions and the c.m. translational energy distributions. The width of the

hyperthermal beam velocity distribution was fit well by a Gaussian function centered at 8262 m s^{-1} and a FWHM of 900 m s^{-1}. This fit was used during data analysis. Note that the data we report for flight times over a 33.7-cm distance were calculated by subtracting the *average* oxygen flight time from the nozzle to the interaction region; the reported product arrival times, then, reflect a convolution of the oxygen beam's wide velocity distribution and the "true" product translational energy distribution, so the best-fit $P(E_T)$ distributions may not be unique. As such, we estimate the uncertainties in the reported $P(E_T)$ distribution to be 10 – 20%.

To allow for easy manipulation of the $P(E_T)$ and $T(\theta_{c.m.})$ distributions, parameterized functions were often used. The fitting process often relied on the RRK form of the $P(E_T)$ distribution:

$$P(E_T) = (E_T - B)^p (E_{avail} - E_T)^q$$

where E_{avail} is the total available energy in the c.m. frame, i.e., the collision energy, E_{coll}, minus the endothermicity, ΔE. The parameters B, p, and q were adjusted to vary the peak and width of the c.m. translational energy distribution when obtaining a best fit to the laboratory data. The $T(\theta_{c.m.})$ distribution was described using a Legendre polynomial form:

$$T(\theta_{c.m.}) = \sum_{k=0}^{n} a_k \frac{1}{2^k k!} \frac{d^k}{dx^k} (x^2 - 1)^k$$

where $x = \cos\theta_{c.m.}$ and a_k is an adjustable parameter for each polynomial term. Eleven terms were used, i.e., k = 0, 1, 2, …, 10. The functional forms for the $P(E_T)$ and $T(\theta_{c.m.})$ distributions were iterated in the XBEAM program until they provided satisfactory fits to the laboratory data. In some cases, point forms of the $P(E_T)$ and $T(\theta_{c.m.})$ distributions were used. Finally, the "best-fit" $P(E_T)$ and $T(\theta_{c.m.})$ distributions were used to create a c.m velocity-flux contour map or a differential scattering cross-section plot for the products.

Theoretical c.m. angular and translational energy distributions for oxygen isotope exchange from 23.1 to 149.9 kcal mol^{-1}

Theoretical c.m. differential scattering cross-sections for the oxygen isotope exchange reaction (Figure S2) showed a preference for backwards scattering at all collision energies. The incident oxygen atom, attached to the product CO_2 molecule, appeared to prefer scattering in a direction opposite its initial direction, i.e., backwards. As the collision energy increased, however, the angular distribution of products showed little qualitative change: Reactively scattered products showed sightly more preference for backwards scattering up to E_{coll} = 149.9 kcal mol^{-1}, the highest collision energy considered in this study.

The theoretical c.m. product translational energy distributions showed significant (≥ 50%) transfer of the available energy into internal degrees of freedom of the products at all collision energies ≥ 57.7 kcal mol^{-1}. The QCT data below E_{coll} = 57.7 kcal mol^{-1}did not contain statistically significant number of reactive trajectories, i.e., > 30, so they were not included in this analysis. $P(E_T)$ distributions became broader as the collision energy increased, though the proportion of energy remaining translation was similar at all collision energies. A bimodal distribution of translational energies may exist in the products of BMK trajectories run at E_{coll} = 57.7, 80.7, and 103.8 kcal mol^{-1}; for instance, separate peaks were observed at ~50% and ~80% of the available energy for the 57.7 kcal mol^{-1} trajectories, although there is considerable uncertainty in the theoretical translational energy distribution (see Figure S2). Additional QCT calculations will be required before structure in the product translational energy distributions can be determined conclusively.

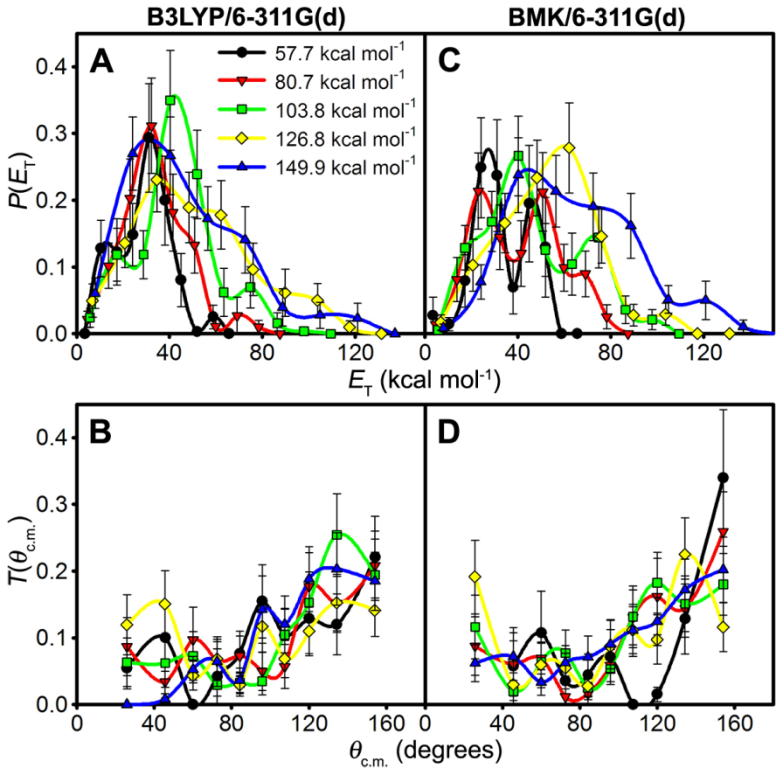

Figure S2. Center-of-mass angular and translational energy distributions for the $O(^3P)$ + CO_2 isotope exchange reaction derived from QCT calculations at the (**A** and **B**) B3LYP/6-311G(d) and (**C** and **D**) BMK/6-311G(d) levels of theory. Distributions with more than 30 reactive trajectories are shown. At both levels of theory and all collision energies shown, reactive scattering shows a preference for backwards scattering ($\theta_{c.m.} > 90°$) with a moderate ($\geq 50\%$) transfer of translational energy to internal degrees of freedom of the products.

Inelastic scattering of $^{16}O_2$ and $^{12}C^{18}O_2$

The hyperthermal oxygen beam contained 13% of molecular oxygen. The scattering of $^{16}O_2$ with $^{12}C^{18}O_2$ was also studied. The experiment mainly observed signals due to $^{16}O_2$ scattered with little deflection from its initial direction (see Newton diagram in Figure S3). Five representative laboratory-frame TOF distributions (m/z = 32), the c.m. angular and translational energy distributions, and the laboratory-frame angular distribution obtained from $^{16}O_2$ product detection are shown in Figure S4. Inelastically scattered $^{16}O_2$ and $^{12}C^{18}O_2$ had 126.3 kcal mol^{-1} total translational energy, or 80% of the available energy (see Figure S4B), on average. The experimental translational energy distribution was peaked at ~148 kcal mol^{-1}. The c.m. angular distribution for $^{16}O_2$ was highly peaked in the forward direction with little scattered intensity for $\theta_{c.m.} > 30°$; however, the velocity and angular range for $^{16}O_2$ product detection in the experiment prevented the detection of backwards-scattered $^{16}O_2$ (see Figure S3). Some dependence of the c.m. translational energy distribution on the c.m. angular distribution was observed in the $^{16}O_2$ TOF data; the forward-convolution simulations became increasingly faster than the data at larger laboratory and c.m. angles (e.g, Θ = 18°, 28°, and 42° in Figure S4A). We also note that, like for ^{16}O, the c.m. angular distribution for inelastically scattered $^{16}O_2$ at $\theta_{c.m.} \sim 0°$ is an extrapolation because of high background from the hyperthermal source at the small laboratory angles corresponding to small c.m. angles for $^{16}O_2$. Most of the $^{16}O_2$ probably scatters forward through high-impact-parameter collisions, but the limited constraints on the $\theta_{c.m.} \sim 0°$ angular distribution (e.g., the laboratory-frame angular distribution, which only probes $\Theta \geq 6°$) increase the uncertainty in that part of the c.m. angular distribution.

Due to the range of detector angles used, the experiment mainly observed $^{12}C^{18}O_2$ scattered opposite its initial direction in the c.m. frame (see Newton diagram in Figure S3). Detected $^{12}C^{18}O_2$ products (m/z = 48) showed best-fit c.m. translational energy distributions that were both broader and lower in energy, on average, than that obtained for forward-scattered $^{16}O_2$. Like for the inelastic scattering of $^{12}C^{18}O_2$ from ^{16}O, a single pair of $P(E_T)$ and $T(\theta_{c.m.})$ distributions was not sufficient to describe the m/z = 48 TOF distributions, and a second pair of $P(E_T)$ and $T(\theta_{c.m.})$ distributions was included in the fit. Five representative laboratory-frame TOF distributions, the c.m. angular and translational energy distributions, and the laboratory-frame angular distribution obtained from $^{12}C^{18}O_2$ product detection are shown in Figure S5**,** along with the c.m. velocity-flux diagram in Figure S6. The first $P(E_T)$ and $T(\theta_{c.m.})$ pair for

inelastically scattered $^{12}C^{18}O_2$ described the scattering at $\theta_{c.m.} < 125°$. In this region, the angular distribution was peaked near $\theta_{c.m.} = 60°$, though the probability of scattered products was roughly constant for $0° < \theta_{c.m.} < 40°$. The probability of finding these products decayed steadily at $\theta_{c.m.} > 60°$. The corresponding translational energy distribution was peaked at 60 kcal mol^{-1} with $\langle E_T \rangle$ = 62.8 kcal mol^{-1}, or 40% of the available energy. The second $P(E_T)$ and $T(\theta_{c.m.})$ pair for inelastically scattered $^{12}C^{18}O_2$ described the scattering at $60° < \theta_{c.m.} < 125°$ (corresponding to the maximum $\theta_{c.m}$ observed in the experiment), although there was a small component $0° < \theta_{c.m.} < 60°$. This angular distribution overlapped, in the sideways-scattering region, with the first pair. For $\theta_{c.m.} > 60°$ the distribution increased rapidly until it peaked near $\theta_{c.m.} = 120°$ and decayed quickly at $\theta_{c.m.} > 120°$. However, this part of the distribution is uncertain because our experiment did not probe it directly. The translational energy distribution was peaked at 103 kcal mol^{-1} with $\langle E_T \rangle$ = 100.8 kcal mol^{-1}, or 64% of the available energy.

The similarity in product c.m. angular and translational energy distributions in the O_2 + CO_2 system and the O(^3P) + CO_2 system suggests that the collisional energy transfer mechanism is similar in both cases. Ryali *et al.*[8] found that CO_2 collisions with N_2, O_2, and Ar at high collision energies all had similar translational-to-vibrational energy transfer cross-sections for the excitation of $CO_2(v_3)$, so they suggested that energy transfer sampled the repulsive part of the intermolecular potential in all cases. Transfer of vibrational energy from O_2 to CO_2 cannot be ruled out in our experiments because we did not characterize the vibrational temperature of the hyperthermal O_2. Consequently, the similarity in inelastic scattering dynamics of O(^3P) and O_2 collisions with CO_2 could also be coincidental.

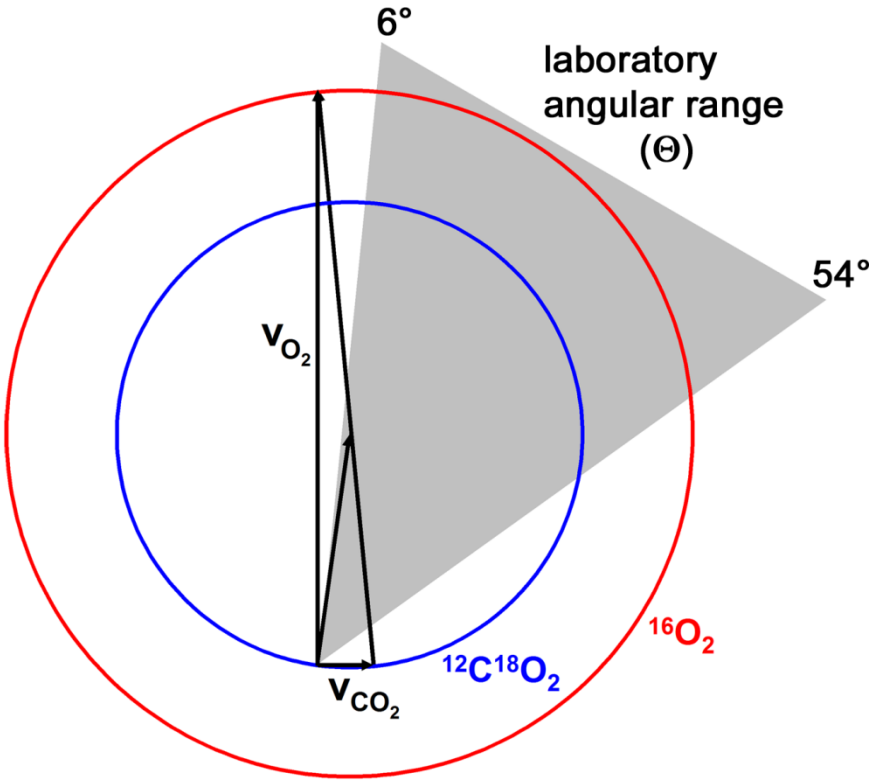

Figure S3. Canonical Newton diagram for inelastic scattering of $^{16}O_2$ + $^{12}C^{18}O_2$. The Newton circles represent the maximum recoil velocities for $^{16}O_2$ and $^{12}C^{18}O_2$ products.

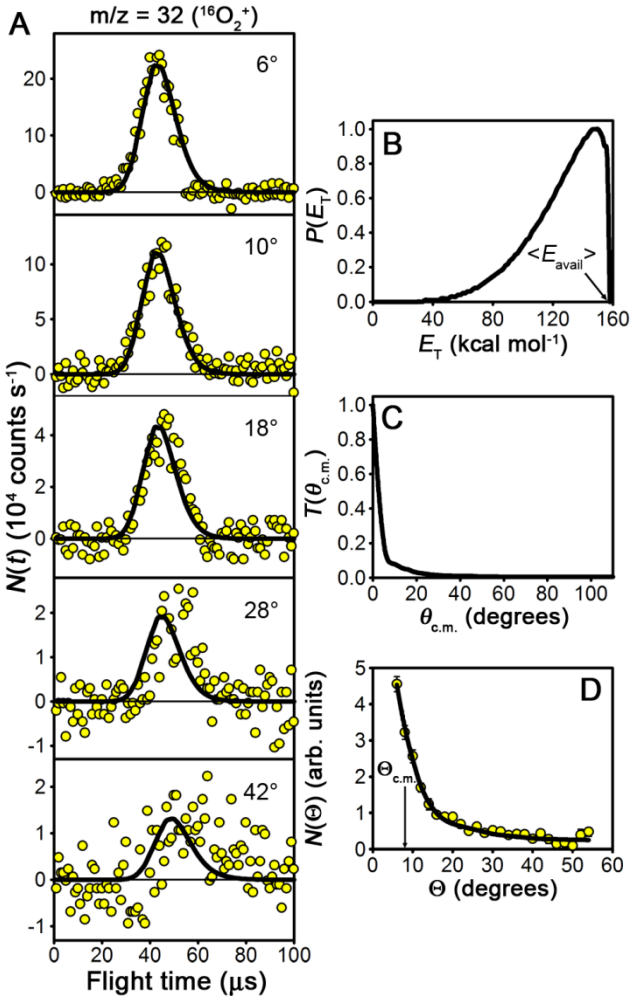

Figure S4. (**A**) Laboratory TOF, (**B**) c.m. translational energy, and (**C**) c.m. and (**D**) laboratory angular distributions for inelastically scattered $^{16}O_2$ products from $^{16}O_2$ + $^{12}C^{18}O_2$ collisions at $\langle E_{coll} \rangle$ = 158.1 kcal mol^{-1}. The circles in (**A**) and (**D**) are experimental data, while the lines are the best-fit forward-convolution simulations of the experimental data derived from the c.m. translational energy and angular distributions shown in (**B**) and (**C**), respectively. The error bars in (**D**) represent 2σ uncertainties in the integrated experimental TOF distributions, which were calculated by using the Monte Carlo method (see Appendix **A**). These data indicate that $^{16}O_2$ is scattered mainly in the forward direction with little change in its initial direction or velocity.

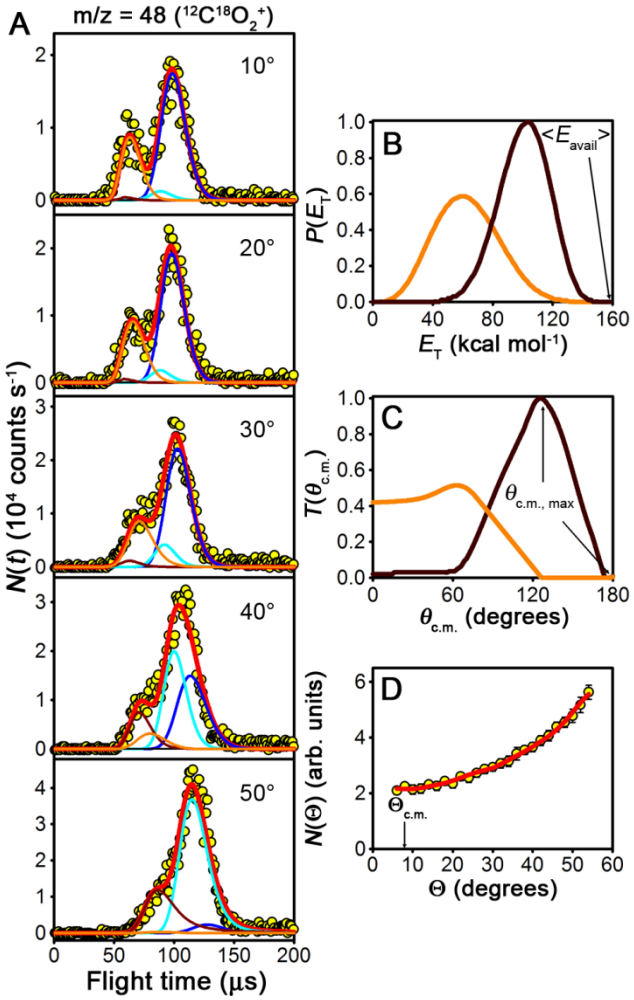

Figure S5. (**A**) Laboratory TOF, (**B**) c.m. translational energy, and (**C**) c.m. and (**D**) laboratory angular distributions for inelastically scattered $^{12}C^{18}O_2$ products from $^{16}O_2$ + $^{12}C^{18}O_2$ collisions at $\langle E_{coll} \rangle$ = 158.1 kcal mol^{-1}. The circles in (**A**) and (**D**) are experimental data, while the lines (orange and brown) are the best-fit forward-convolution simulations of the experimental data derived from the c.m. translational energy and angular distributions shown in (**B**) and (**C**), respectively; the maximum $\theta_{c.m.}$ to which the experiment is sensitive is noted in (**C**). The error bars in (**D**) represent 2σ uncertainties in the integrated experimental TOF distributions, which were calculated by using the Monte Carlo method (see Appendix **A**). In (a), the main peak at ~100 to 120 μs in the TOF distributions are inelastically scattered $^{12}C^{18}O_2$ products from ^{16}O + $^{12}C^{18}O_2$ collisions at $\langle E_{coll} \rangle$ = 98.8 kcal mol^{-1}. The corresponding c.m. angular and translational energy distributions can be found in Figure 6 of the main manuscript (dark blue and cyan lines). A single c.m. translational energy and angular distribution for each collision partner was insufficient to describe the TOF distributions of inelastically scattered $^{12}C^{18}O_2$, suggesting a scattering dependence on impact parameter.

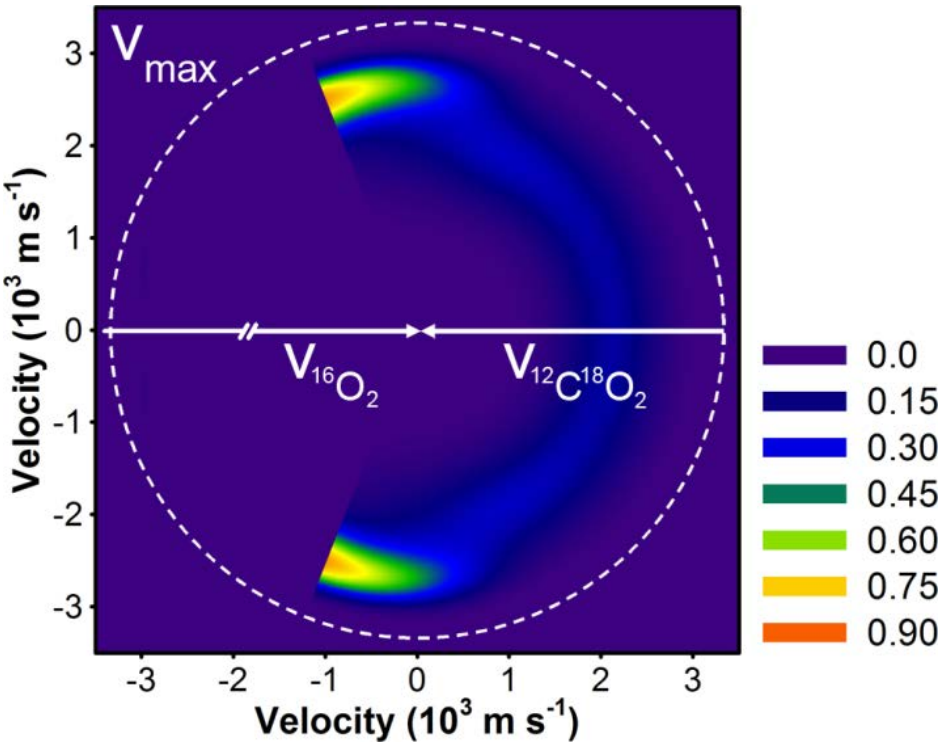

Figure S6. Velocity flux contour diagram for inelastically scattered $^{12}C^{18}O_2$ from $^{16}O_2$ + $^{12}C^{18}O_2$ collisions in the center-of-mass frame. The white arrows are the initial $^{16}O_2$ and $^{12}C^{18}O_2$ velocity vectors and the dashed white line is the maximum recoil velocity for $^{12}C^{18}O_2$ (v_{max}). Only the c.m. angles for which the experiment were sensitive are shown. Strong coupling of the $P(E_T)$ and $T(\theta_{c.m.})$ distributions was observed.

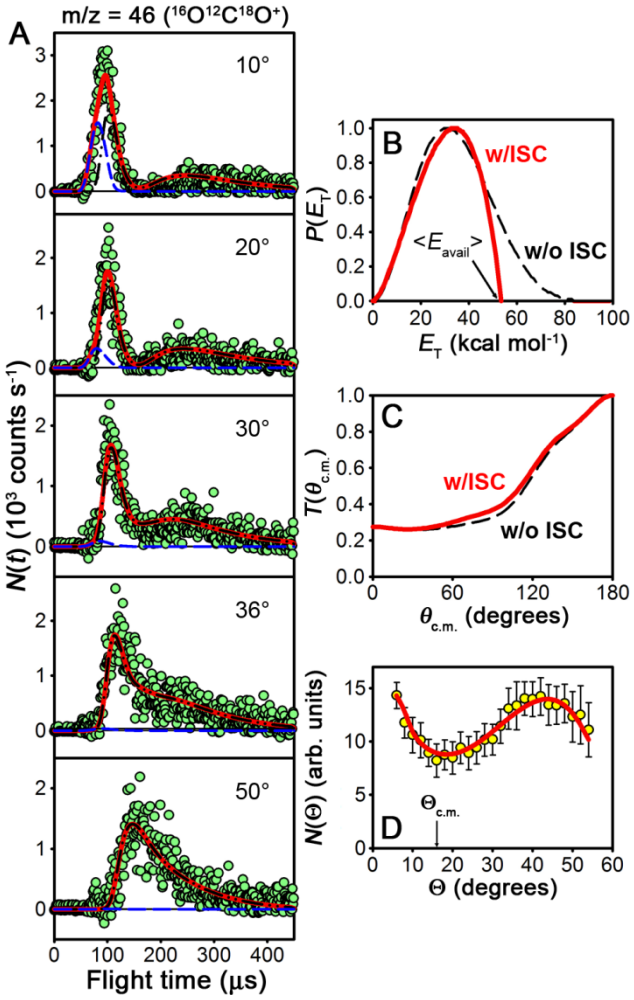

Figure S7. (**A**) Laboratory TOF, (**B**) c.m. translational energy, and (**C**) c.m. and (**D**) laboratory angular distributions for reactively scattered $^{16}O^{12}C^{18}O$ products from the $^{16}O(^3P)$ + $^{12}C^{18}O_2$ → $^{18}O(^1D)$ + $^{16}O^{12}C^{18}O$ reaction at $\langle E_{coll} \rangle$ = 98.8 kcal mol^{-1}. The circles in (**A**) and (**D**) are experimental data, while the lines are the best-fit forward-convolution simulations of the experimental data derived from the c.m. translational energy and angular distributions shown in (**B**) and (**C**), respectively. The forward-convolution fits included ~45 kcal mol^{-1} endothermicity of $O(^1D)$ vs. $O(^3P)$ due to intersystem crossing (ISC). Center-of-mass translational energy and angular distributions without ISC are also shown in (B) and (C) for comparison. The dashed lines in (**B**) and (**C**) are the best-fit c.m. translational energy and angular distributions without ISC. The peak and average of the $P(E_T)$ distribution with ISC in (**B**) were 34 and 30.7 kcal mol^{-1} (63% and 58% E_{avail}), respectively. In (**A**), the best-fit forward-convolution simulations of $^{16}O^{12}C^{18}O$ products from $^{16}O(^3P)$ + $^{12}C^{18}O_2$ collisions (black dot-dashed lines) are shown with those from $^{16}O_2$ + $^{12}C^{18}O_2$ collisions at $\langle E_{coll} \rangle$ = 158.1 kcal mol^{-1} (blue dashed lines).[9] The error bars in (**D**) represent 2σ uncertainties in the integrated experimental TOF distributions, which were calculated by using the Monte Carlo method as described in Appendix **A**.

Animated Trajectories

DirectExchange_CO3.mwv Oxygen isotope exchange through a short-lived CO_3 intermediate.

ComplexExchange_CO3.mwv Oxygen isotope exchange through a longer-lived CO_3 intermediate.

ComplexAbstraction_18-O2.mwv Oxygen-atom abstraction through a CO_3^*-complex mechanism that would result in $^{18}O_2$ products experimentally.

ComplexAbstraction_16-18-O2.mwv Oxygen-atom abstraction through a CO_3^*-complex mechanism that would result in $^{18}O^{16}O$ products experimentally.

References

(1) Karton, A.; Rabinovich, E.; Martin, J. M. L.; Ruscic, B. *J. Chem. Phys.* **2006**, *125*, 144108.

(2) Karton, A; Daon, S; Martin, J. M. L. *Chem. Phys. Lett.* **2011**, *510*, 165.

(3) Lee, T. J.; Taylor, P. R. *Int. J. Quantum Chem.* **1989**, *Symp. 23*, 199; Lee, T. J.; Rice, J. E.; Scuseria, G. E.; Schaefer III, H. F. *Theor. Chim. Acta* **1989**, *75*, 81.

(4) Lee, T. J. *Chem. Phys. Lett.* **2003**, *372*, 362; Leininger, M. L.; Nielsen, I. M. B.; Crawford, T. D.; Janssen, C. L. *Chem. Phys. Lett.* **2000**, *328*, 431; Janssen, C. L.; Nielsen, I. M. B. *Chem. Phys. Lett.* **1998**, *290*, 423; Nielsen, I. M. B.; Janssen, C. L. Chem. Phys. Lett. **1999**, *310*, 568.

(5) Karton, A.; Martin, J. M. L.; Taylor, P. R. *J. Chem. Phys.* **2007**, *127*, 064104.

(6) Caledonia, G. E.; Krech, R. H.; Green, B. D. *AIAA J.* **1987**, *25*, 59.

(7) Lee, Y. T. Reactive Scattering I: Nonoptical Methods. In *Atomic and Molecular Beam Methods*; Scoles, G., Ed.; Oxford University Press: New York, 1988; Vol. 1; pp 533.

(8) Ryali, S. B.; Fenn, J. B.; Kolb, C. E.; Silver, J. A. *J. Chem. Phys.* **1982**, *76*, 5878.

(9) Yeung, L. Y.; Okumura, M.; Paci, J. T.; Schatz, G. C.; Zhang, J.; Minton, T. K. *J. Am. Chem. Soc.* **2009**, *131*, 13940.